A Large Basin on the Near Side of the Moon

Charles Joseph Byrne

Abstract   The differences between the surface structure of the near side and the far side of the Moon have been topics of interest ever since photographs of the far side have been available. One recurrent hypothesis is that a large impact on the near side has deposited ejecta on the far side, resulting in thicker crust there. Specific proposals were made by P.H. Cadogan for the Gargantuan Basin and by E.A. Whitaker for the Procellarum Basin. Despite considerable effort, no consensus has been reached on the existence of these basins. The problem of searching for such a basin is one of finding its signature in a somewhat chaotic field of basin and crater impacts. The search requires a model of the topographic shape of an impact basin and its ejecta field. Such a model is described, based on elevation data of lunar basins collected by the Lidar instrument of the Clementine mission and crustal thickness data derived from tracking Clementine and other spacecraft. The parameters of the model are scaled according to the principles of dimensional analysis and isostatic compensation in the early Moon. The orbital dynamics of the ejecta and the curvature of the Moon are also taken into account. Using such a scaled model, a search for the best fit for a large basin led to identification of a basin whose cavity covers more than half the Moon, including the area of all of the impact basins visible on the near side. The center of this basin is at 22 degrees east longitude and 8.5 degrees north latitude and its average radius is approximately 3,160 km. It is a megabasin, a basin that contains other basins (the far side South Pole-Aitken Basin also qualifies for that designation). It has been called the Near Side Megabasin. Much of the material ejected from the basin escaped the Moon, but the remainder formed an ejecta blanket that covered all of the far side beyond the basin rim to a depth of from 6 to 30 km. Isostatic compensation reduced the depth relative to the mean surface to a range of 1–5 km, but the crustal thickness data reveals the full extent of the original ejecta. The elevation profile of the ejecta deposited on the far side, together with modification for subsequent impacts by known basins (especially the far side South Pole-Aitken Basin) matches the available topographic data to a high degree.

C. J. Byrne (✉)
Image Again, 39 Brandywine Way, Middletown, NJ 07748, USA
e-mail: charles.byrne@verizon.net

The standard deviation of the residual elevations (after subtracting the model from the measured elevations) is about one-half of the standard deviation of the measured elevations. A section on implications discusses the relations of this giant basin to known variations in the composition, mineralogy, and elevations of different lunar terranes.

Keywords Moon · Lunar basins · Multi-ringed basins · Multi-ring basins · Impact basins · Basin ejecta · Clementine · Near Side Megabasin · South Pole-Aitken Basin

1 Introduction

1.1 How the Far Side Differs from the Near Side

Before spacecraft visited the far side of the Moon we expected that it would look like the near side (Fig. 1).

The former Soviet Union launched spacecraft that successfully photographed the Moon's far side: Luna 3 in October 1959 and Zond 3 in July 1965. The American spacecraft Lunar Orbiter 1, launched in August 1966, improved the picture quality (Fig. 2) and the rest of the Lunar Orbiter missions covered nearly all of the far side.

The photos these spacecraft returned showed us quite another picture of the far side of the Moon than we had expected. Instead of dark and light areas, we saw a very uniform scene, mostly bright, like the near side highlands. There were just a very few dark mare areas. Yet the terrain was very heavily bombarded, with craters and basins overlapping


Fig. 1 The near side of the Moon. This picture has its contrast enhanced to emphasize the strong patterns of dark mare against bright highlands (Lunar and Planetary Institute, LPI)

Fig. 2 The western far side of the Moon, looking back to Earth. This picture extends from beyond what we see as the eastern limb to nearly the center of the far side. This picture is a mosaic made from Lunar Orbiter photos LO1-116 M and LO1-117M (LPI). The mosaic has been made from photos that have been processed to remove artifacts of scanning and reconstruction (Byrne 2002, 2005, 2008)

each other. A comparison of Fig. 2 with the familiar sight in Fig. 1 indicates the degree of difference in the two sides of the Moon.

Photographs from the mapping camera in the Apollo Command Module reinforced the observations of the unmanned missions, as shown in the Fig. 3. It shows the eastern limb of
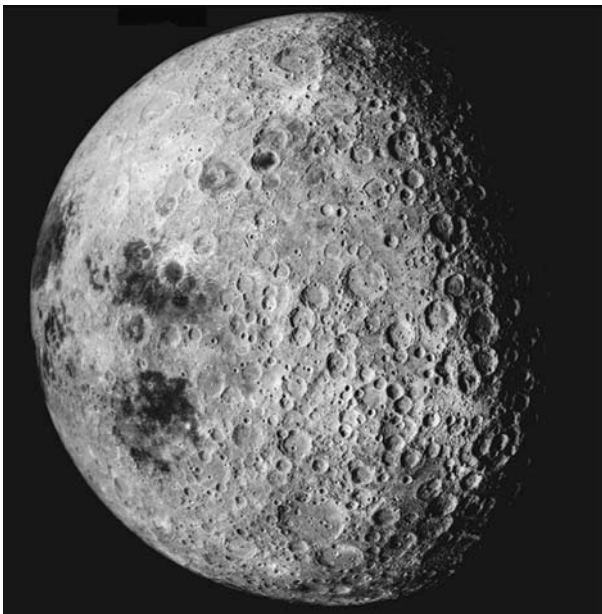

Fig. 3 The eastern limb of the Moon. Mare Smythii and, above that, Mare Marginis, are mostly on the near side. The far side is to the right (NASA, Apollo photo a16_m_3021, LPI)

the Moon, with the near side on the left and the far side on the right. The relative ruggedness of the far side terrain is clear.
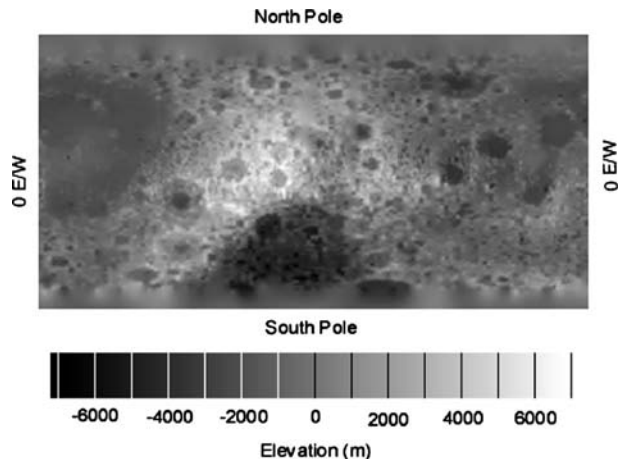
1.2 The South Pole-Aitken Basin

As we gained information about the Moon from the Clementine mission (Nozette et al. 1994) of the Navy Research Laboratory (NRL) and the Lunar Prospector mission of the National Aviation and Space Agency (NASA) we learned more about the giant South Pole-Aitken Basin on the far side. The depth of this basin had been previously discovered from Zond3 and Apollo laser altimetry, and various observers gradually realized its scope (Wilhelms 1987), but the Clementine mission revealed its full scope. This basin extends from the South Pole up to about 10 degrees south latitude (Figs. 4, 5).

Fig. 4 Elevation map of the Moon, centered on the near side. This geographic map displays elevation as a gray scale against latitude from 90 degrees south to 90 degrees north and longitude from 180 degrees west to 180 degrees east. The data (called topogrd1) was derived from the Clementine LIDAR instrument (Zuber et al. 2004). NRL
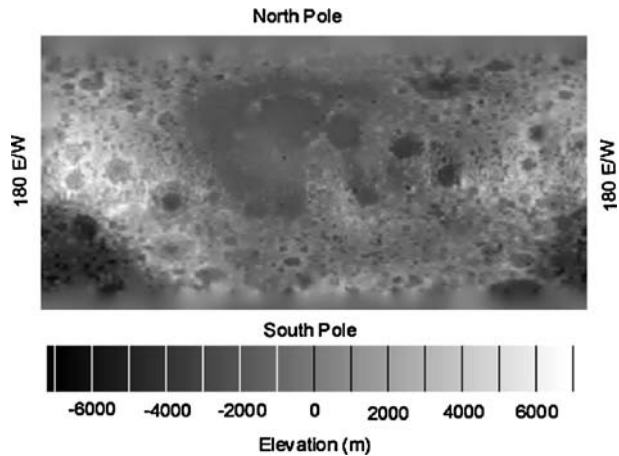
Fig. 5 This elevation map is like that of Fig. 4 except that it is centered on the far side. The dark depression is the South Pole-Aitken Basin. The large Korolev Basin is just north of the South Pole-Aitken Basin, at the top of the farside bulge. NRL

1.3 The Far Side Bulge

The Clementine altimeter confirmed that the Moon is irregularly shaped, with a bulge of several kilometers in elevation, covering most of the far side north of the South Pole-Aitken Basin.

1.4 Moments of Inertia

The moments of inertia of the Moon have been measured from its physical libration and are known to be non-conformant to moments that would be caused by an equatorial bulge that accompanies current or former rotation (Garrick-Bethell et al. 2006).

1.5 Gravity Field and Crustal Thickness

Analysis of the gravity field of the Moon, as measured by tracking of orbital spacecraft, determined that the thickness of the crust is greater on the far side than on the near side (Zuber et al. 1994; Neumann et al. 1996; Hikida and Wieczorek 2007). Further, the center of mass of the Moon is displaced about 2 km toward the near side, relative to the center of the figure of its surface (Zuber et al. 1994).

1.6 Composition and Elemental Abundance

The Lunar Prospector mission (Binder 1998) provided additional evidence of the unusual surface distributions of relatively heavy elements like titanium (Elphic et al. 2002), iron (Lawrence et al. 2002), and thorium (Lawrence et al. 2000; Gasnault et al. 2002). A useful set of maps can be found in Busey and Spudis (2004). Nearly all areas with elevated levels of these metals are found on the near side of the Moon, the eastern limb of the Moon, and in the South Pole-Aitken Basin (Garrick-Bethell 2004). The highest concentrations are in the mare that flood large basins on the near side, but those highlands that have relatively low elevations, specifically the central highlands on the near side, also have high levels of heavy metals. Earlier evidence from sample return and remote sensing indicated a similar distribution of KREEP (Lucey et al. 2006), a mix of radioactive decay products and incompatible elements, those that are concentrated by re-melting processes (Wieczorek and Phillips 2000). These materials tend to be more abundant at the surface of the near side, especially near Oceanus Procellarum and the Imbrium Basin (Lucey et al. 1994), but in a lesser degree to the southeast. The distribution led to a suggestion that it could be accounted for by the addition of a second large basin to the Procellarum Basin, this one centered at 5° south and 65° east (Feldman et al. 2002).

1.7 Hypotheses for the Cause of Asymmetry

J.A. Wood (Wood 1973) reviewed the evidence of asymmetry of the Moon and suggested that moments of inertia, crustal variations, center of gravity, and bulging topography could all have been produced by a combination of impacts and the effect of Earth's gravity early in the Moon's history.

P.H. Cadogan (Cadogan 1974) and E.A. Whitaker (Whitaker 1981) each proposed that a large impact had hit the near side, creating a basin much larger than the known basins and spreading its ejecta on the far side. Cadogan proposed a set of coordinates and the name "Gargantuan Basin" and Whitaker proposed coordinates for a larger basin with the name "Procellarum Basin". The boundaries of these proposed basins each use the arc of the west edge of Oceanus Procellarum. Despite considerable support, the topographic evidence did not confirm their proposed boundaries. Further, an examination of the crustal thickness model derived from Clementine data (Neumann et al. 1996) could not support the proposed morphology of the Procellarum Basin.

Recently, it has been proposed (Garrick-Bethell et al. 2006) that a strong asymmetry could have been induced if the Moon, still soft, could have been in a very elliptical orbit, in a 3:2 synchronism between the orbital and spin periods. This hypothesis does not explain the lateral differences in thickness of the crust, the shift in center of mass, or the heavy element distribution.

Several proposed mechanisms for generating asymmetry in the course of the Moon's evolution (Lucey et al. 1994) have been classified in Feldman et al. (2002). For example, a thicker far side crust might have been generated by bombardment, preferentially focused on the near side of a Moon in synchronism by the gravity of Earth. However, a study of the ejecta from the currently known basins (Petro and Pieters 2004, 2005) shows that ejecta collects around clusters of the basins, not away from them.

In accordance with the ideas of J.A. Wood, this paper reports on the successful search for a very large near side basin that is quantitatively consistent with both the elevation and crustal thickness evidence from the Clementine mission. The size and shape of the ejecta from this giant near side basin match both the far side topograpy and crustal thickness, when the effects of isostatic compensation are considered. The relation to compositional asymmetry and the shift between center of mass and center of figure is addressed in Sect. 7.1.

2 Data Sources

Two digital elevation maps were downloaded from the web page of the Washington University at St. Louis (Zuber et al. 2004). One map, Topogrd2, has 0.25° separation between data points and the other, Topogrd1, has 1.0° separation (Figs. 4, 5). Both were used in the course of this work. The data is derived from a combination of tracking data of the Clementine spacecraft and measurements from its LIDAR laser altimeter (Zuber et al. 1994). A limitation of the LIDAR data is that is imprecise within 12° of each pole.

The methods of inferring crustal thickness from variations in the gravity field are described in Neumann et al. (1996). The variations are determined from their effects on spacecraft data, measured by tracking. Assumptions of density (Hikida and Mizutani 2005) and measurements of topography are used to derive the thickness of the underlying crust. The data that was used here (Fig. 21) was described in Hikida and Wieczorek (2007). Dr. Hikida provided a digital map (1° separation) to this author.

3 A Model for Impact Basins

The first step in the search for a large near side basin was to form a generalized, scalable model of an impact basin. The shape of impact features scale with size (Melosh 1989). Key

equations used in the model are presented in this section. In some cases, there are references to derivations in the Appendix.

3.1 Scaling by Dimensional Analysis

Through a discipline called dimensional analysis, impacts of all sizes can be compared to normalized models (Housen et al. 1983). It was necessary to extrapolate the model beyond the size of previously known basins, the largest of them being the South Pole-Aitken Basin. As in any case of extrapolation, one must be watchful for new phenomena that disrupt the scaling rules. In this case, one such effect was encountered: the ejection ballistics could not be approximated by parabolas and were modeled by orbital ellipses. This was done for both the South Pole-Aitken Basin and the proposed near side basin. Another modification that was needed was to separate depth and diameter by using double normalization. With these modifications, the remaining scaling rules were confirmed.

3.2 Depth/Diameter Ratio and Double Normalization

Dimensional analysis rules constrain the depth of an impact cavity to be proportional to its diameter for the gravity regime where the strength of the material is negligible. However, this assumes that the characteristics of the target material are constant, not a reliable assumption for all lunar impact features. Target properties may differ in location or composition. Impact features might have undergone different degrees of isostatic compensation, which would change the depth/diameter ratio. Further, there is a dependency on size. The depth/diameter ratio is found to be approximately constant for lunar craters less than 10 km but there is a much smaller constant of proportionality for larger diameters (Williams and Zuber 1998). The result is that the depth/diameter ratio decreases with diameter beyond 10 km. The physical reason for this is unknown.

Therefore, no specific correlation has been assumed here between diameter and depth of impact craters. Each basin has been doubly normalized by measured diameter and estimated depth for generation of the model.

The radius is normalized on R_A, the radius corresponding to the *apparent diameter* of the internal cavity, where the observed cavity intercepts the estimated target surface. The depth is normalized on d_T, the *true depth* between the estimated target surface and the center of the cavity before fill by mare or other material. The estimates are made from a radial profile of each feature. The italicized terms are those of Turtle et al. (2005). There has been some controversy over whether the radius of the physical transient cavity (the radius of pulverized, molten, and vaporized minerals) may be smaller or larger than R_A. This paper applies the scaling laws to R_A but takes no position on the question of whether it is the radius of the subsurface transient crater.

The depth and diameters of the sample basins discussed in this paper are presented in Table A.1 and Fig. A.3 of the Appendix, along with a discussion of how their depths have affected by target characteristics.

3.3 Radial Profiles

The model of Fig. 6 shows averaged radial profiles of several lunar basins that are first measured using Clementine elevation data and then normalized by both depth and diameter. Each profile represents the elevation, averaged over 360 degrees of azimuth, as a function of radius from the center of each basin (Byrne 2006a). This approach reduces the erratic effects of subsequent impact features, scalloping and landslides at the rims, and radial ridges and troughs in the ejecta blanket.

3.4 Removal of the Elevation and Curvature of the Target Surface

The various profiles in Fig. 6, are not taken directly from an elevation map. It is necessary to estimate and remove the elevation and curvature of the target surface during the process of normalization. The curvature (relative to the geoid) came about because of preceding events on the Moon. In particular, an impact on the exposed cavity of a large previous basin encounters negative curvature and an impact in previous ejecta encounters positive curvature. As an example, consider the radial elevation profile of the Korolev Basin (Fig. 7). That basin formed on top of the bulge on the far side. The profile of the bulge must be subtracted from the elevation profile in order to derive the characteristic shape of an impact basin that would results from a strike on a flat target (Fig. 8).

The average radial profile of an impact feature can be thought of as a general model of such features combined, through superposition, with characteristics of the target surface. The parameters of the model are the apparent radius R_A (from the center to the intercept of the cavity with the target surface) and the true depth d_T (from the bottom of the estimated cavity before fill to the target surface). The measured average radial profile at the target surface can be represented by a Taylor's series expansion, $a + br + cr^2 + ...$, where r is the radius from the center. Term b, the slope, is removed by averaging over azimuth and is not a consideration. Terms a (target elevation at the center) and c (target

Fig. 6 The solid line is a radial profile of a generalized impact basin. The light lines are radial profiles of seven lunar basins ranging from 400 km to 900 km in diameter. Some of these basins have inner and outer rings and have been partially filled with mare. The sample basins were measured using the 0.25° database topogrd2 (Zuber et al. 2004). See Table A.1 in the Appendix for the dimensions of these basins
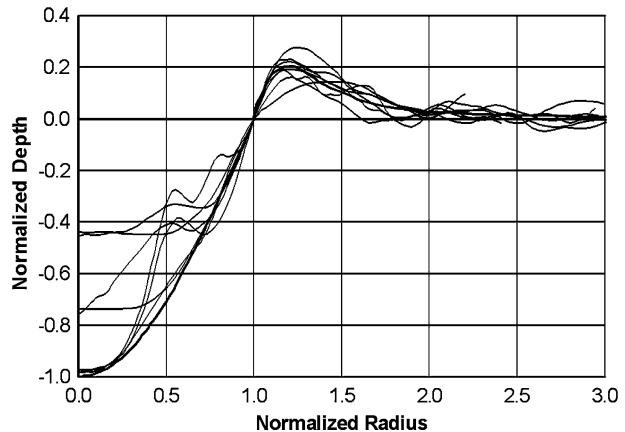
Fig. 7 The gray curve is the averaged radial elevation profile of the Korolev Basin. The solid line is an estimate of the elevation and curvature of the original target surface
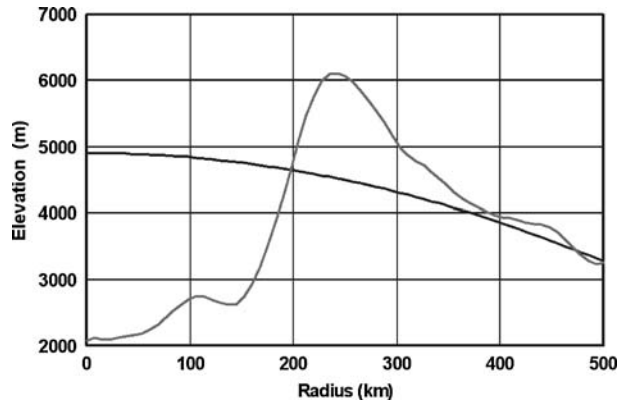
Fig. 8 After subtraction of the estimated elevation and curvature, the gray line represents the averaged radial depth profile of Korolev if it had been formed in a flat target surface at 0 km elevation. The black curves are the model profile fitted to the Korolev data. They show Korolev's mare fill, exposed slope, rim, and ejecta blanket. Korolev has a single inner ring that has been partly covered by mare
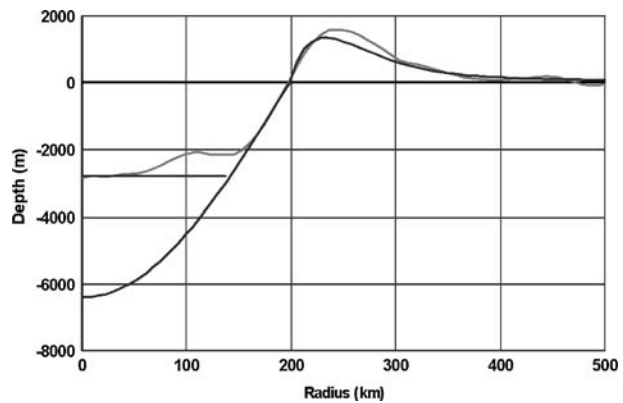
curvature) are estimated from the measured averaged radial profile. I used an interactive software program to set parameters R_A, d_T, a, and c by trial and error to achieve the following goals:

- Parameter a is set so that the ejecta depth goes toward zero beyond the edge of the ejecta blanket.
- The cavity follows a cosine curve, modified by inner and intermediate rings if present, by mare fill, and by ejecta deposited by neighboring features.

The exposed slope between the rim and any floor fill and inner rings is consistent with the depth estimate. The elevation of the top surface of the mare is directly measured, not estimated from mare depth.

Figures 7 and 8 illustrate the process of estimating elevation and curvature. Figure 7 shows the averaged radial profile of the current topography around the center of the Korolev Basin. Figure 8 shows how Korolev would appear today if it had struck a flat surface at the reference elevation. If isostatic compensation is suspected, then the vertical scale of the feature must be changed to estimate its depth just after the impact.

After subtraction of the estimated elevation and curvature, the gray line represents the averaged radial depth profile of Korolev if it had been formed in a flat target surface at 0 km elevation. The black curves are the model profile fitted to the Korolev data. They show Korolev's mare fill, exposed slope, rim, and ejecta blanket. Korolev has a single inner ring that has been partly covered by mare.

3.5 Model of the Cavity

Despite the variations in fill level and internal rings, a negative cosine curve fits the envelope of the cavity of the normalized radial profiles very well. The equation for this curve is:

$$Z_c = -Cos(R_i \cdot \pi/2) \tag{1}$$

where Z_c is the normalized central depth after collapse of the transient crater (estimated, if there is fill) and R_i is the normalized radius within the apparent crater.

The cosine curve is a better match to internal basins that are fully exposed and free of internal rings than a parabolic curve. The depths of the two curves are within 10%, but the cosine curve is a better fit to the slope that rises to the rim. This region is very important in the estimation of depth, because it is often exposed even if much of the cavity is filled with mare or, in the case of the two giant basins, regenerated crust. Mare and internal rings are superimposed on that curve and are modeled separately as required.

3.6 Model of the Ejecta Field

If our only objective were to model the typical basins on the Moon, we could make an empirical model of the rim and ejecta blanket that fits the normalized basins. But our objective is to have a model that would not only fit the South Pole-Aitken Basin and also to search for an even larger basin on the near side. To model such large basins, it is necessary to find a normalized velocity profile that would produce an ejecta pattern that would fit that of the measured radial profiles. Then that velocity profile could be used to predict the range that ejecta is thrown, when the trajectory cannot be approximated by a simple parabolic trajectory.

The equations that control the relation between ejection and deposit are described in Ivanov (1976). As the transient crater expands during the dissipation of impact energy, each annular ring of incremental radius throws an incremental volume of ejecta outward at a velocity that depends on the launch radius in magnitude. This spray of ejecta is called an ejection cone. The ejecta from an incremental annular ring wihin the cavity falls on an incremental annular ring outside the cavity that depends on the range of ejection, which in turn depends on the ejection velocity.

The scaling rules (Housen et al. 1983) provide that the launch angle is constant (typically about 45 degrees in laboratory experiments) as the radius changes, and so is the incremental volume of ejecta per increment of radius.

The rate of ejected volume with radius is proportional to ejection area (Appendix A.1):

$$dV_i/dR_i = V_0 \cdot R_i^2 \tag{2}$$

where V_i is the normalized volume that has been ejected from the cavity as a function of normalized radius R_i of the expanding shock wave and V_0 is a constant whose value fits the radial profiles.

The magnitude of the velocity (speed) varies strongly with the radius of launch, being very high near the point of impact and falling to zero at what will become the edge of the impact basin. The function shown in Fig. 9 is empirical (see the appendix for its detailed description), but it is asymptotic to the theoretical curve based on dimensional analysis near the center of the impact. In this region, which produces the far field of ejecta, the magnitude of the velocity (speed) is (Appendix A.12):

$$S_f = 0.73 \cdot R_i^{-2.6} \tag{3}$$

The coefficient 0.73 and the exponent 2.6 are optimal for the features examined. The exponent is in accord with experimental data on similar materials. An energy balance equation (Richardson 2007) fits the empirical function of Fig. 9 from the center to 0.93 of the normalized radius within 2.6%. The ejecta in this range falls beyond 1.28 of the normalized radius, just beyond the rim: thus the fit of the energy balance equation is good for the ejecta blanket, but not for the rim, where other considerations dominate.

The range between ejection and deposit can be calculated by the familiar parabolic ballistic equation (Appendix A.2):

$$r_b = 2 \cdot (s_i^2 / G_m) \tag{4}$$

where r_b is the range of deposit from the ejection radius, s_i is the magnitude of the velocity of ejection, and the angle of ejection is assumed to be 45°.

After the velocity profile was established, the launch angle was found to vary between 40° and 50° with little effect.

The radius of deposit is given by (Appendix A.7):
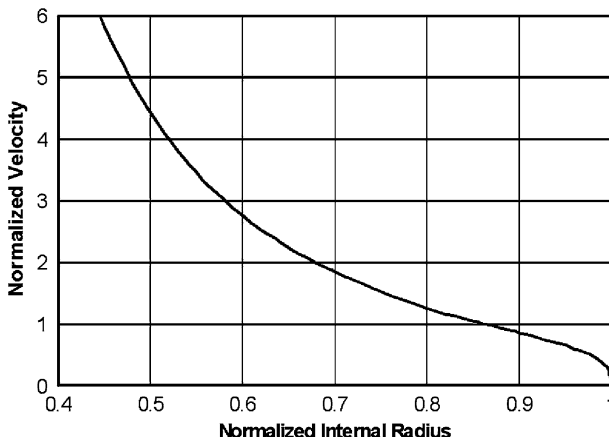
Fig. 9 This radial profile of the magnitude of ejection velocity (ejection speed), together with the assumptions supported by dimensional analysis and experiment, produces the model ejecta pattern of Fig. 6. The normalized peak elevation of the rim in the model, 0.205 above the target surface, and the normalized radius of that rim, 1.20, have been set at the average of the radial profiles of these 54 impact features. The volume of ejecta of the model is greater than that of the modeled cavity. The difference is attributed to about 10% greater porosity in the ejecta

$$R_e = R_i + R_b \tag{5}$$

3.7 Depth of Deposited Ejecta

Numerical analysis was performed to solve the equations of ejection, range, and the circumference of the incremental ring of deposit. The depth of deposited ejecta is given by (Appendix A.9):

$$Z_e = Z_r(R_i/R_e)/(dR_e/dR_i) \tag{6}$$

where Z_e is the depth of the ejecta deposit.

Since the velocity profile is empirical, the ejecta depth must be derived by numerical analysis. The V_0 parameter described above and the shape of the normalized velocity profile were varied until the shape of the deposited ejecta was an acceptable match to the set of radial profiles. Initially the selected set of seven basins was used, but then the velocity profile was adjusted to match the average depth and diameters of the rims of the larger sample of a total of 54 basins and large craters. A presentation of the equations above, with supporting figures, is given in Ivanov (1976).

At this point, the model had been developed so that it could successfully model any basin or crater between the sizes of Tycho and the Imbrium Basin, provided that there was not an extremely oblique impact (the angle of impact was at least 30° above the horizontal).

3.8 Effects of Megabasin Ejecta Trajectories

The model of an impact basin and its ejecta shown in Fig. 6 fits the medium-sized basins, but could not be expected to fit a megabasin of the size of the South Pole-Aitken Basin or larger because of the spherical shape of the Moon and its gravity field. For the smaller basins, the gravity vector was approximated by a normal to a flat surface, yielding a parabolic ejecta trajectory. But actually the ejecta is launched in either an elliptical orbit (if it returns to the Moon) or a hyperbolic trajectory (if it escapes). Then the range, if the trajectory is not hyperbolic, is given by (Appendix A.15):

$$r_b = 2R_m \tan^{-1}\left[\frac{\left(s_i^2/R_m \cdot G_m\right) \cdot \sin A \cdot \cos A}{\left(1 - (s_i^2/R_m \cdot G_m) \cdot \cos^2 A\right)}\right] \tag{7}$$

where r_b is the range between the radius of ejection and the radius of deposit, s_i is the ejection speed, R_m is the radius of the Moon, G_m is the Moon's gravity at its surface, and A is the angle of launch. The equation above is quoted in Melosh (1989) and the derivation is in Thomson (1986).

3.9 The Spherical Target and Antipode Effect

Another important difference between the ejecta pattern of very large basins and medium basins is that the area available for an incremental ring of ejecta to occupy shrinks as the ejecta falls toward the antipode. On an approximately flat surface, the depth of an incremental ring of ejecta deposited at a given radius from the center is simply its incremental

volume divided by the product of the width of the ring and the circumference of a circle of the given radius. But when the basin is so large that its ejecta must be considered as falling on a spherical surface, the circumference of the circle is reduced.

Accordingly, the ejecta depth equation for the flat target case must be modified by the following correction factor to compensate for the decrease in circumference (Appendix A.16):

$$C = Sin(r_i/R_m)/Sin(r_e/R_m) \tag{8}$$

where the correction factor C approaches r_i/r_e when the target radius is much larger than the impact feature.

When the ejecta, in its orbit, reaches the antipode of the impact point at π radians, the ejecta from all directions converges (theoretically) at a point and the depth would be infinite.

Of course, variations from the assumptions and the dynamic angle of repose actually spread the ejecta out somewhat in the vicinity of the antipode, especially since the ejecta is deposited at the same angle as it was ejected (45°). As it lands, it retains a large horizontal velocity. Slopes of the antipode mound can be further reduced by isostatic compensation.

3.10 Isostatic Compensation

The hypothesized giant impact may have occurred very early in the history of the Moon, so early that the Magma Ocean had not fully solidified. If so, both the ejecta blanket and the cavity would have undergone isostatic compensation (Neumann et al. 1996; Wieczorek and Phillips 1998; Wieczorek et al. 1999). The weight of the added crust ejected from a giant basin on the near side would have forced the primitive crust beneath it into the mantle on the far side, and the mantle on the near side would have pressed upward on the cavity and compressed it.

Assumptions about the density of the crust and mantle (Hikida and Wieczorek 2007) imply that complete isostasis would reduce initial topography to stable topography by a factor of 6.0. The Airy model of isostasy relates that factor to density as follows:

$$Z_{iso} = Z_0 \cdot (3.36 - 2.8)/3.36 = Z_0/6.0 \tag{9}$$

where Z_0 is an initial elevation variation, Z_{iso} is the variation after complete compensation, 3.36 gm/cm^3 is the density of the mantle, and 2.8 gm/cm^3 is the density of the crust (Hikida and Wieczorek 2007).

The reasoning that led to the density assumptions can be found in Hikida and Mizutani (2005).

At this point, there was a sufficiently sophisticated model to search for a basin even larger than the South Pole-Aitken Basin.

4 The Near Side Megabasin and the South Pole-Aitken Basin

With a general model of an impact basin in hand, the search for the basin that has left its debris on the far side could proceed. The search was conducted by varying the model's

parameters (latitude and longitude of the center, the diameter, and the depth) until a best match to the measured lunar surface was found. The criterion of the best match was to minimize the standard deviation of the residual after the model was subtracted from the Clementine topogrd1 elevation data (1° resolution). The measurement of standard deviation was limited to the region between 78 degrees south latitude and 78 degrees north latitude because the LIDAR data is not reliable near the poles. Initially, the South Pole-Aitken Basin was not modeled, but in a later stage, it was. The result was that a single new impact basin could account for most of the evidence of topographic asymmetry.

To do its work, the new impact basin had to be very large indeed. In fact, its cavity covered more than half the Moon. Its center is in the western part of Mare Tranquillitatis, not far from the Apollo 11 landing, but its rim is on the far side. The radius is more than half way around the Moon. All of the mare areas of the near side are within this basin. Since it includes many smaller basins, I refer to it as the Near Side Megabasin (Byrne 2006b, 2008). The South Pole-Aitken Basin also has smaller basins within it and could be described as the far side megabasin.
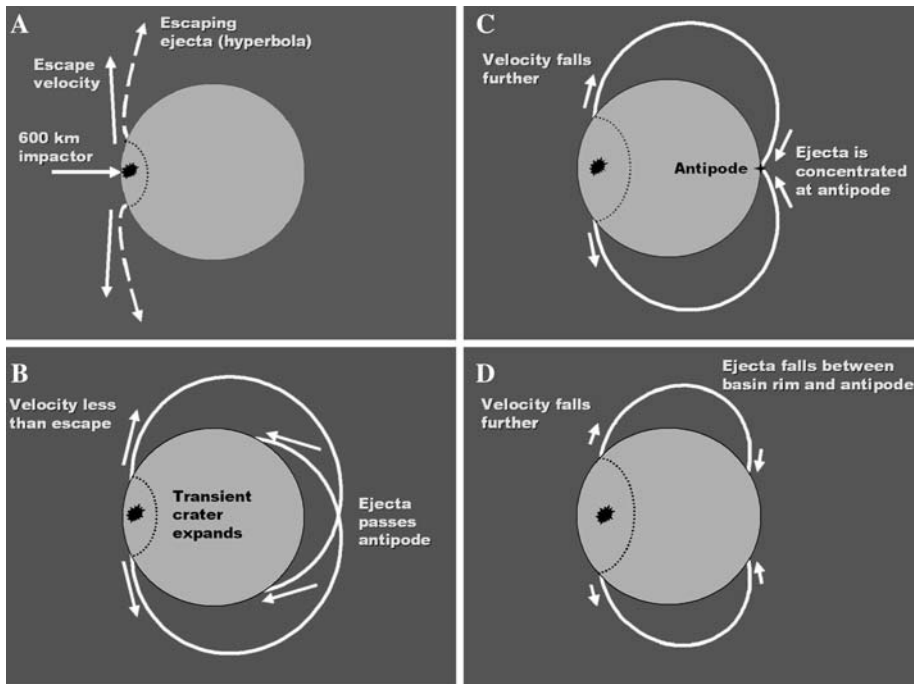
When the parameters of the Near Side Megabasin and the South Pole-Aitken Basin were adjusted, these two basins and their ejecta explained the gross shape of the Moon. The bulge on the far side was centered on the antipode of the Near Side Megabasin. After impact, the bulge had been roughly symmetrical about the antipode. Then the impact of the South Pole-Aitken Basin modified the southern sector of the bulge by emplacing its cavity there. This complex pattern of the two interacting basins probably contributed to the difficulty in perceiving the Near Side Megabasin at an earlier time.

The impacts that caused the two megabasins were each so violent that much of the material ejected from each basin had escape velocity, and was lost to the Moon. The volumes of ejecta from the Near Side Megabain and the South Pole-Aitken Basin, as a function of radius from the point of impact to the rim, are shown in Fig. 10.

Note that most of the ejecta from the Near Side Megabasin escaped the Moon, at least initially (perturbations in the Earth-Moon system may have returned some of it to the Moon). The ejecta pattern of the Near Side Megabasin is unlike that of any other basin, not because the dynamics of its transient crater and internal cavity are any different, but simply
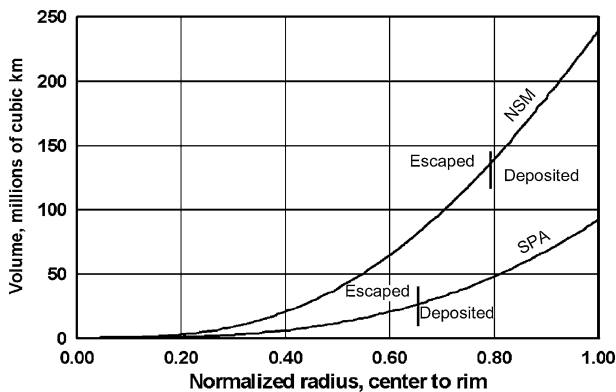
Fig. 10 Cumulative volumes ejected from the Near Side Megabasin and the South Pole-Aitken Basin, based on circular models. The volumes are derived from the velocity profile

Fig. 11 This series of qualitative sketches shows the evolution of the Near Side Megabasin as its transient crater expands. (**a**) The diameter of the impactor of the Near Side Megabasin may have been as large as 600 km, assuming that it was about one-tenth of the basin diameter. The initial ejection velocity, appropriately scaled, would have been greater than the lunar escape velocity. (**b**) As the transient crater expands, the velocity falls below escape velocity. Ejecta is deposited inside of a specific boundary, a scarp, that is nearly circular. The orbits are not to scale; their apolunes are much larger than shown. (**c**) As the transient crater grows further, the ejection velocity falls further and (at a specific time after impact) the ejecta all falls together at the antipode, producing the center of the far side bulge. Since a ring of ejected material falls at a point (the antipode) the depth there would be unbounded if the velocity of the deposited ejecta did not have a horizontal component (falling, as it rose, at about 45° inclination). This effect disperses the deposited ejecta over a finite area. The same effects that produce radial ridges and troughs vary the amount of deposits from different azimuths, so opposing horizontal momenta do not cancel out. (**d**) As the transient crater expands, the ejecta lands on the region between the antipode and the expanding cavity. Ultimately, the launch ring and the deposit ring meet as the velocity falls to zero at the edge of the Near Side Megabasin

because of its enormous size, relative to its spherical target. The manner of the deposit is shown in Fig. 11, followed by a set of elevation maps that are centered on the cavities and antipodes of the two giant basins (Fig. 12).

4.1 Maps of the Two Giant Basins

The two giant basins are difficult to visualize because of their scale and the unusual shapes of their ejecta blanket. Figure 12 shows Lambert equal area elevation maps that are centered on the centers and antipodes of these basins.
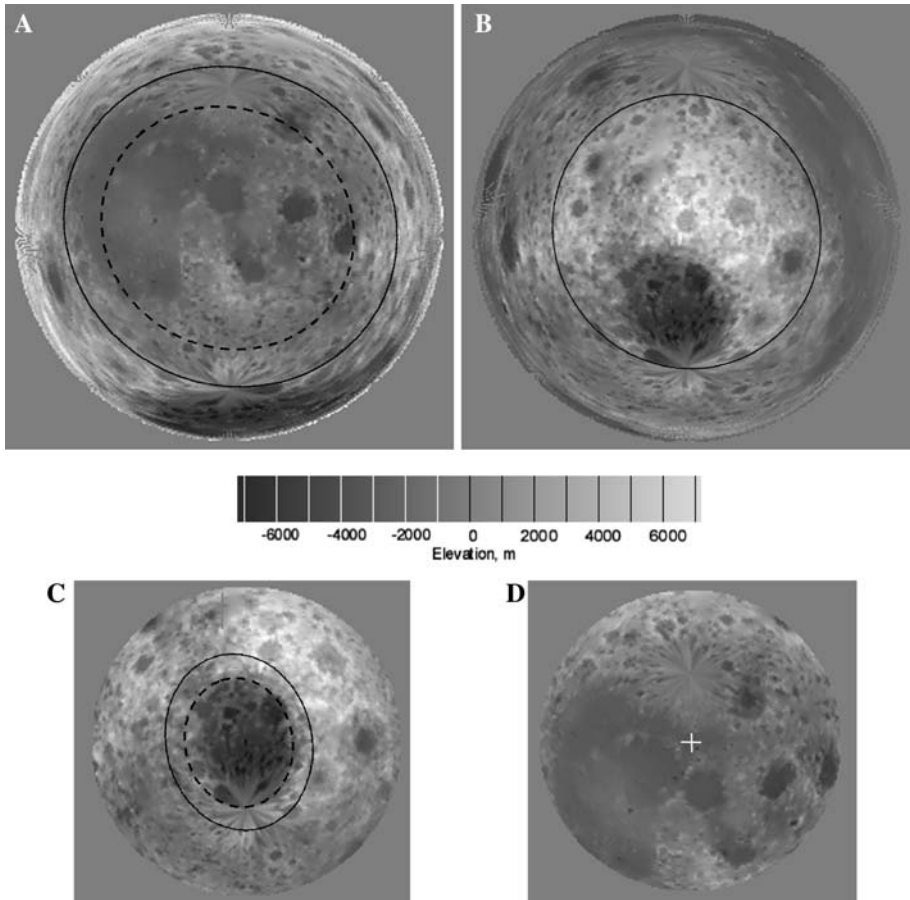
Fig. 12 Elevation Maps of the two giant basins. (**a**) Lambert equal area projection, centered on the cavity of the Near Side Megabasin, 150° range. The solid ellipse is the boundary of the apparent crater (intersection of the cavity with the estimated target surface). The rim and ejecta are on the far side, outside of the solid ellipse. The dashed ellipse is the boundary of the flat floor. (**b**) Lambert equal area projection, centered on the antipode of the Near Side Megabasin, 150° range, on the far side of the Moon. The antipode is in the southwest quadrant of the Korolev Basin, whose rim is in white. The solid ellipse is the boundary of the apparent crater of the Near Side Megabasin. The rim and ejecta blanket are inside of this ellipse. (**c**) Lambert equal area projection, centered on the cavity of the South Pole-Aitken Basin, 90° range. The solid ellipse is the boundary of the apparent crater. The rim and ejecta are outside of the solid ellipse. The dashed ellipse is the boundary of the flat floor. (**d**) Lambert equal area projection, centered on the antipode of the South Pole-Aitken Basin, 90° range. The white cross marks the antipode, in Mare Frigoris. The ejeccta is not obvious here because its depth never exceeds 150 m, except possibly at the antipode

4.2 The Far Side Bulge and the Korolev Basin

The bulge on the far side of the Moon shown clearly in the elevation map of Fig. 12b was caused by the heavy double layer of ejecta that fell into the limited region near the antipode point. It formed a peak at the antipode. We cannot see that peak now, because a subsequent impact formed the Korolev basin; the antipode is well within that basin. The radial profile of Korolev on top of the antipode mound can be seen in Fig. 7.
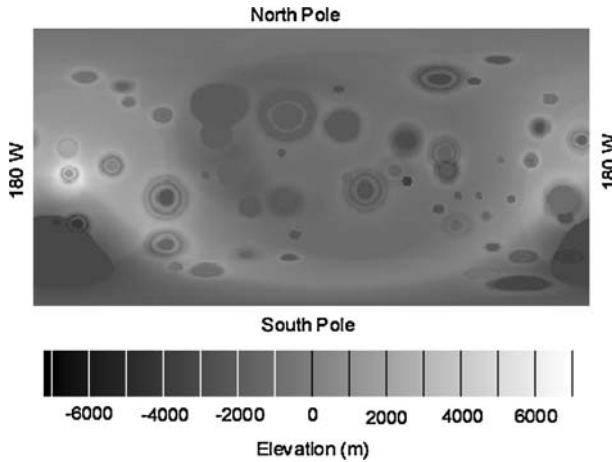
Fig. 13 This is the proposed model of the Moon. It includes, in sequence, the Near Side Megabasin, the South Pole-Aitken Basin, the crust in the internal basin of the Near Side Megabasin, 54 smaller basins and large craters, mare fill in the craters, and the Oceanus Procellarum depression (see Sect. 7.4). The models of the two giant basins include the effect of isostatic compensation

5 Model Compared to Measurement

The detailed model that includes the Near Side Megabasin (after full isostatic compensation) is shown in Fig. 13. The parameters of the Near Side Megabasin that minimize the residual standard deviation are shown in Table 1.

The pattern of ejecta caused by the model of the Near Side Megabasin is in close quantitative agreement with the measured radial profile, centered on the cavity (see Fig. 14). The depression at the antipode of the Near Side Megabasin (the point 180° from its center) is due to the presence of the Korolev Basin (Fig. 7).

The measured profile of Fig. 14 excludes the southeastern sector that would include the South Pole-Aitken Basin's cavity. However, deposits from that basin in other sectors contribute to the average radial profile. A horizontal line represents the crust that has refilled the floor of the basin. Above the crust is a considerable amount of ejecta from basins that have been formed by subsequent impacts.

The scarp caused by the drop in ejecta velocity from escape to deposit is 140 m according to the model, and an indication of it can be seen in the radial profile. The scarp has been exposed to the history of bombardment of the far side and can no longer be a sharp cliff, even if chaotic factors did not diffuse it when the upper ejecta layer was deposited. Examination of Lunar Orbiter photographs of the area of the scarp did not show unambiguous visual evidence of it.
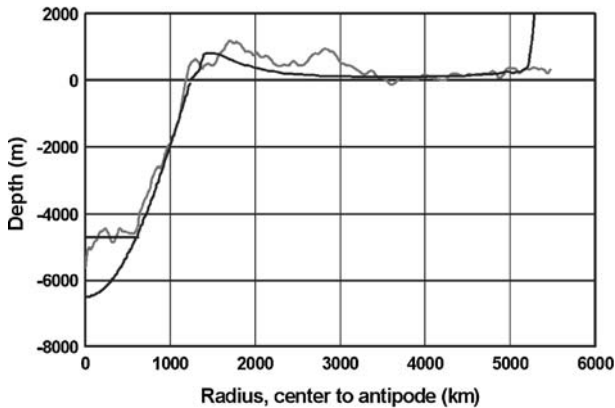
Table 1 The Near Side Megabasin

* Initially, before isostatic compensation, 21 km

Latitude	8.5° North	Longitude	22° East
Major axis	3,320 km	Minor axis	3,013 km
Depth	3.5 km*	Launch angle	50° from flat
Eccentricity	0.42	Orientation	53° W. of N.
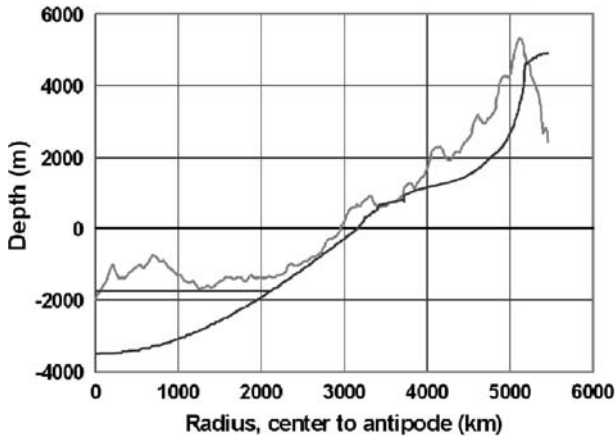
Fig. 14 The radial profile of the Near Side Megabasin, from center to antipode. The rough curve is an average radial profile and the smooth curve is the model (including isostatic compensation). Near the antipode, the rough curve shows the approximate profile of Korolev, whose center is near the antipode of the Near Side Megabasin. The smooth curve shows the estimated elevation and curvature of the Korolev target surface (Fig. 7)


Fig. 15 The radial profile of the South Pole-Aitken Basin is compared to the model

The level floor of the Near Side Megabasin is due to refilling of the basin from below, probably by new crust, rather than mare material. Above that level fill, the measured curve includes deposits from the South Pole-Aitken Basin. On top of the refilled crust and the deposits from the South Pole-Aitken Basin lie ejecta from later basins.

5.1 The South Pole-Aitken Basin

The radial profile and the model of the South Pole-Aitken Basin are compared in Fig. 15. The parameters of this basin are summarized in Table 2.

The averaging by azimuth of the radial profile is circular, while the basin is actually elliptical. This causes the dual peak of the rim profile, one at the major axis and one at the
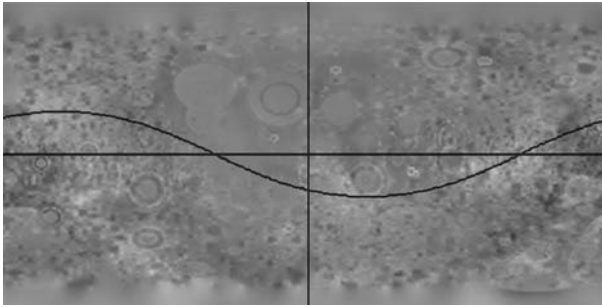
Fig. 16 This is the residual elevation after the model is subtracted from the Clementine elevation map (topogrd1)

Table 2 The South Pole-Aitken Basin			
Latitude[a]	54.2° South	Longitude[a]	168.7 West
Major axis	1,440 km	Minor axis	1,042 km
Depth	6.8 km[b]	Launch angle	42° from flat
Eccentricity	0.69[a]	Orientation[a]	7.5° W. of N.

[a] Garrick-Bethell (2004)

[b] Initially, before isostatic compensation, 40.8 km

minor axis. This dual peak is also in a radial profile of crustal thickness (Neumann et al. 1996). The peak at the antipode is theoretical. Both chaotic variations from symmetry and relaxation to the angle of repose would diffuse it in practice. The antipode cannot be observed directly, because it is beneath Mare Frigoris. However, a thinning of the mare is indicated by the exposure of the rims of craters near the antipode.

When we look at the far side, nearly all that we see has been deposited there from the Near Side Megabasin or is the effect of the South Pole-Aitken Basin or subsequent impacts. Only a few outbreaks of mare are found on the far side, beyond the cavity of the South Pole-Aitken Basin. Most of the geometry of the far side must be understood as evolving from the Near Side Megabasin; its rim, its ejecta blanket, the antipode mound, and the scarp resulting from the transition between ejecta returned to the Moon and ejecta sent into space.

Both giant basins have flat floors, like basins and craters flooded with mare, but in view of sample analysis and remote sensing data, these floors are likely to be reconstituted crust rising from melts in the underlying transient craters. No curvature was assigned to the Near Side Megabasin, suggesting that the primitive surface conformed to the geoid.

5.2 Residual Elevation Map

The map of the residual elevation, the topography left after comparing the model of Fig. 14 to the current elevation is shown in Fig. 16.

The large scale elevation variation in Fig. 16 is much reduced in comparison to the current topography as shown in Fig. 4 but the small-scale residuals due to the smaller craters that have not been modeled is still at the same level. The largest pattern of residuals

Table 3 Standard deviations

	Far side	Near side	Both
Topogrd1	2,633 m	1,200 m	2,135 m
Residual	1,284 m	881 m	1,101 m

is a set of positive features that lie along a great circle (black line) whose northern pole is at 62.5° N and 34° E.

The comparison of standard deviations is shown in Table 3.

The standard deviation of the residual topography (Table 3) is reduced by more than half on the far side and nearly half over both sides. The variance of the residual is only about a quarter of the variance of the current topography.

5.3 Treatment of Basin Eccentricity

The Near Side Megabasin was found using a circular basin model (Byrne 2006b). The South Pole-Aitken Basin was described as an elliptical basin (Garrick-Bethell 2004). This suggested that the Near Side Megabasin might also be elliptical.

Eccentricity was accommodated in the numerical model by allowing the apparent radius to vary with azimuth. Although this approach would not be realistic for a highly elliptical basin, it seems like a reasonable way to treat basins of moderate eccentricity. This approximation was carried out for both the Near Side Megabasin and the South Pole-Aitken Basin and resulted in a further reduction of the residual standard deviation and determination of the elliptical parameters of the Near Side Megabasin.

This treatment does not address several issues associated with ejecta from oblique impacts. Typically, the ejecta blanket is asymmetrical; an oblique impact throws more ejecta downstream from the impact point. Also, an elliptical apparent cavity is not centered at the point of impact. The center of an elliptical cavity is downstream from the point of impact. The center of ejection, assumed here to be the center of the ellipse, may move downstream as the ejection cone expands.

An attempt has been made to model the asymmetry of the ejection field of the two giant basins. The depth was multiplied by a factor that depends on azimuth:

$$Z_a = [1 + O \cdot \cos(Az \cdot \pi/180)] \cdot Z_e$$

where Z_a is a depth whose asymmetry depends on the free obliquity parameter O (O is not the eccentricity of the cavity but a free parameter, to be assigned empirically).

This simple function should reduce the residual standard deviation, if the proper values of O were assigned to each giant basin. The result for the South Pole-Aitken Basin was that the optimal value of O was 0.06 (south to north) and there was a reduction in the residual standard deviation of 0.018%, not a significant amount. The result for the Near Side Megabasin was that the optimal value of O was 1.0 (southeast to northwest). This value implies that there was no upstream ejecta directly along the major axis at all. There was a reduction in the standard deviation of 1.2%. This is a respectable reduction, based on the experience with introducing other parameters.

However there are two residual features along the major axis of that basin, a positive anomaly downstream to the northwest (part of the suspected great circle of positive anomalies) and a negative anomaly upstream to the southeast (a cluster of small craters). The asymmetric term may have been acting to model these features.

Perhaps improved elevation data and separate modeling of the anomalous features may resolve this issue in the future. For the present, the model of asymmetry of the ejecta fields of these two giant basins cannot be said to have conclusive results.

5.4 Summary of Key Assumptions

Several assumptions were made in order to complete the analytic model. The assumptions are:

1. Superposition of lunar impact features (the elevation of a model is added to that of models of all preceding features).
2. Scalability of lunar basins and large craters according to the rules of dimensional analysis except for the depth to diameter ratio (see assumption 5). Because of the size of the Near Side Megabasin and South Pole-Aitken Basin, the trajectories of ejecta have been calculated as elliptical orbits rather than using the parabolic approximation that is appropriate for smaller impact features.
3. Constancy of the angle of launch of ejecta, from the center of an impact feature to its rim.
4. Constancy of the dimensional analysis rule for the production of the volume of ejecta from near the center of an impact feature to its rim.
5. Since the ratio of the observed depth to diameter is partly a function of the target material and partly of the history of subsequent isostatic compensation, no rule is imposed.
6. The models of the South-Pole Aitken Basin and the Near Side Megabasin have elliptical shapes. The internal depressions and ejecta of these models derive from allowing the values of the apparent radius to be a function of azimuth.
7. The Near Side Megabasin and South Pole-Aitken Basin have undergone full Airy isostatic compensation.

These assumptions are believed to be reasonable approximations, and their value is confirmed by the successful reduction in the standard deviation of residual elevations.

6 Sequence of Impacts and Isostatic Compensation

At an early time, the Moon may have been symmetric. Nearly spherical, but with some equatorial bulge due to its rotation, it would have had a crust about 47 km thick over mantle, with a small core.

Then came the impact of the Near Side Megabasin (Fig. 17). Then another impact formed the South Pole-Aitken Basin (Fig. 18). This profile, along the great circle that connects the centers of the two giant basins and their antipodes; shows the interaction between the two basins. The Moon was still plastic, so complete isostatic compensation took place (Fig. 19). Figure 20 shows the current topography along the great circle at a larger scale.

As shown in Fig. 20, the South Pole-Aitken Basin is deeper than the Near Side Megabasin, even though it is much smaller. A possible reason for this unusual situation is that it impacted in an area of ejecta and the rim of the Near Side Megabasin, a region of deep, fractured porous material. The Near Side Megabasin, however, impacted the pristine
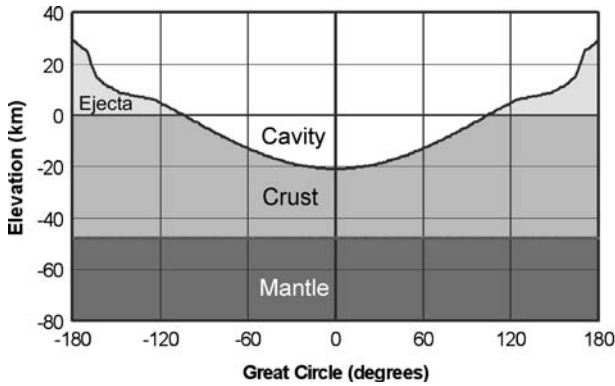
Fig. 17 The Near Side Megabasin struck an apparently uniform layer of crust, piling a mound of ejecta at its antipode
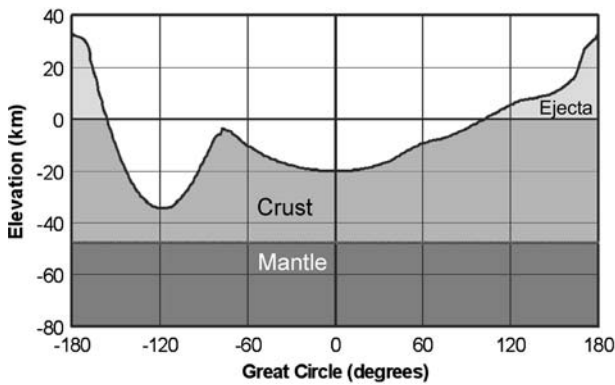

Fig. 18 This profile is along the great circle that connects the centers of the two giant basins and their antipodes. It shows the superposition of the South Pole-Aitken Basin on the Near Side Megabasin. The elevation variation z_0 is as it would have been if the Near Side Megabasin did not undergo significant isostatic compensation before the South Pole-Aitken event. The crustal thickness variations are also z_0
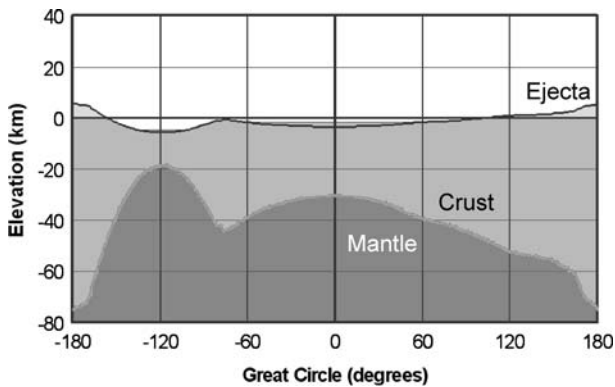
Fig. 19 In time, the mantle pushed upward to compress the ejection cavities and the piles of ejecta pushed the mantle downward, leaving a surface variation (z_{iso}) only one-sixth of the initial variation z_0 (see Eq. 9). The crustal thickness variations in this figure are still as they were before isostatic compensation
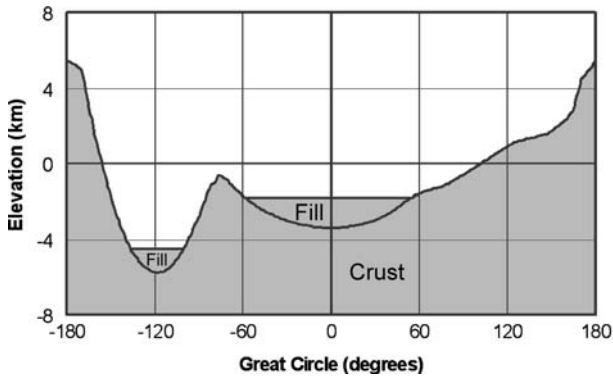
Fig. 20 This scaled-up figure shows the current topography of the Moon. At some time, crustal material has intruded into the cavities and provided level floors, a small part of the isotostatic compensation

crust, which had separated from the Magma Ocean and the target material would have been unfragmented and of low porosity.

The Moon is not completely asymmetric; the hemispheres on either side of the great circle connecting the centers of the two basins are approximately mirror images in topography and crustal thickness.

This topography has provided the substrate for the further developments; bombardment, and mare flows.

7 Discussion

7.1 Asymmetry of the Crustal Thickness, the Center of Mass, and the Moments of Inertia of the Moon

The large-scale topography, allowing for isostatic compensation and ejecta that escapes from the Moon, is compatible with the large-scale crustal thickness. The Moon's center of mass and its three moments of inertia (Garrick-Bethell et al. 2006) could be calculated from the assumed densities of Hikida and Wieczorek (2007) and the crustal thickness map of that paper. This might determine whether the crustal thickness alone (allowing for the mass of mare and a central core) explains the unusual dynamic parameters of the Moon or whether additional density variations are required.

7.2 The Central Highlands and the Crustal Fill

The greater part of the internal basin of the Near Side Megabasin has been refilled to form a level surface, much like that of mare. However, both returned rock samples and remote sensing show this material to be crust unless covered with mare. It is possible that this fill material was formed from a melt of mixed crust and mantle material that

was re-melted by the energy released in the transient crater of the Near Side Megabasin. The central highland region is an exposure of this crust that has escaped basin impacts.

7.3 Residual Heights

After modeling the Near Side Megabasin, there remains a residual of high elevations, including one area in the central highlands (see Fig. 16). The majority of these heights are in a great circle around the Moon that does not correlate with any known feature. Examination of Lunar Orbiter photographs (Byrne 2005) shows that the visual texture of these heights is broadly dispersed, rather than distinct. Two possible explanations come to mind:

1. This great circle belt could be evidence of a fossil bulge, formed when the Moon was spinning faster than it is now (Garrick-Bethell et al. 2006), with its axis somewhat tilted.
2. Material sent from the central region of the Near Side Megabasin in ejection cones at velocities beyond the escape velocity could have been perturbed while in Earth's gravity field and returned to the Moon. If such ejecta formed a ring around the Moon and then collapsed, the debris would have fallen in a great circle.

7.4 The Oceanus Procellarum Depression

There is a depression in the area of Oceanus Procellarum, in the Procellarum KREEP terrane but it does not appear to be an impact basin. Rather, it is shaped like a narrow horseshoe, turned on its side (see Figs. 4, 12a). The bend is at Oceanus Procellarum, the northern arm continues into Mare Frigoris, and the southern arm continues to the Humorum and Nectaris basins. As a speculation, this depression may result from the crust sinking into the space vacated by mare material that flows into the large basins in this region. The crust there may have been extensively fractured by sonic energy originating from the South Pole-Aitken impact (Schultz 2007).

An analysis of this region (Wieczorek and Phillips 2000) finds evidence of a very large pool of re-melted mantle that was 500 km deep, reaching down to the seismic discontinuity.

7.5 Elemental Distribution

The Near Side Megabasin and the South Pole-Aitken Basin, between them, encompass nearly all of the areas of elevated abundance of heavy elements and KREEP within their cavities. Outside the cavities of these two giant basins, the Moon is devoid of elevated concentrations of these materials, with rare exceptions like Mare Moscoviense and the mare within the Tsiolkovskiy crater.

It is possible that these materials were brought near the surface by turbulence within the transient cavities of the giant basins (Ivanov 2007) and then carried to the surface by mare flows.

The Near Side Megabasin encompasses both large basins that were suggested by analysis of the distribution of heavy elements, as measured by Lunar Prospector and

Clementine remote sensing data (Feldman et al. 2002). An ellipse, the Near Side Megabasin neatly envelops the two proposed large circular basins, whose centers were roughly along the major axis. The two smaller basins, even though large, could never have accounted for the topography and crustal thickness on the far side as does the Near Side Megabasin; their ejecta blanket would have fallen on the near side, the poles, and the limbs.

7.6 Revised Terranes

Several papers have characterized major types of asymmetry as different compositional units or terranes on the basis of distributions of elements, elevation, or crustal thickness (Lucey et al. 1994; Neumann et al. 1996; Jolliff et al. 2000). In light of the proposed Near Side Megabasin, the different terranes could be characterized as follows:

1. The exposed melt sheets of the Near Side Megabasin and the South Pole-Aitken Basin, sloping from their flat floors to their rim.
2. The flat floors of the two giant basins, refilled with regenerated crustal material after the primitive crust was thinned by ejection.
3. The area outside of the cavities of the two giant basins, composed of a layer of primitive crust (about 47 km), ejecta from the Near Side Megabasin (5–30 km thick), and ejecta from the South Pole-Aitken Basin (1–5 km). These layers are in isostatic equilibrium so that the topography is reduced by a factor of 6.0 from the crustal thickness.
4. Mare basalt from the mantle, re-melted by radioactivity, floods the floors of deep basins and some large craters. These flows are preferentially within the cavity of the Near Side Megabasin because of the size of its transient crater.
5. The Procellarum KREEP Terrane (Jolliff et al. 2000), a region of very highly concentrated heavy elements that has undergone re-melting, resulting in extensive flooding of mare basalt, even overflowing some basins (Byrne 2004).
6. Deposits of crustal material along a great circle that is not correlated with any other features. Perhaps this material has returned from being ejected at greater than lunar escape velocity from the giant basin, and been returned to the Moon after being retained in unstable orbits within the Earth-Moon system.

8 Summary

The similarity of the current topography, crustal thickness reduced to topography by isostasy, and the model including the Near Side Megabasin is shown in Fig. 21.

The major conclusion of this paper is that the Near Side Megabasin, a newly described single impact basin, produced most of the large-scale asymmetry of the Moon's topography and crustal thickness. Internal asymmetries of the primitive crust and mantle are not required. In order to produce both the current topography and crustal thickness maps, both the Near Side Megabasin and the South Pole-Aitken Basin must have been fully isostatically compensated (Zuber et al. 1994).

The three representations of current topography of Fig. 21 summarize the quantitative agreement between the model and both topographic and crustal thickness measurements.
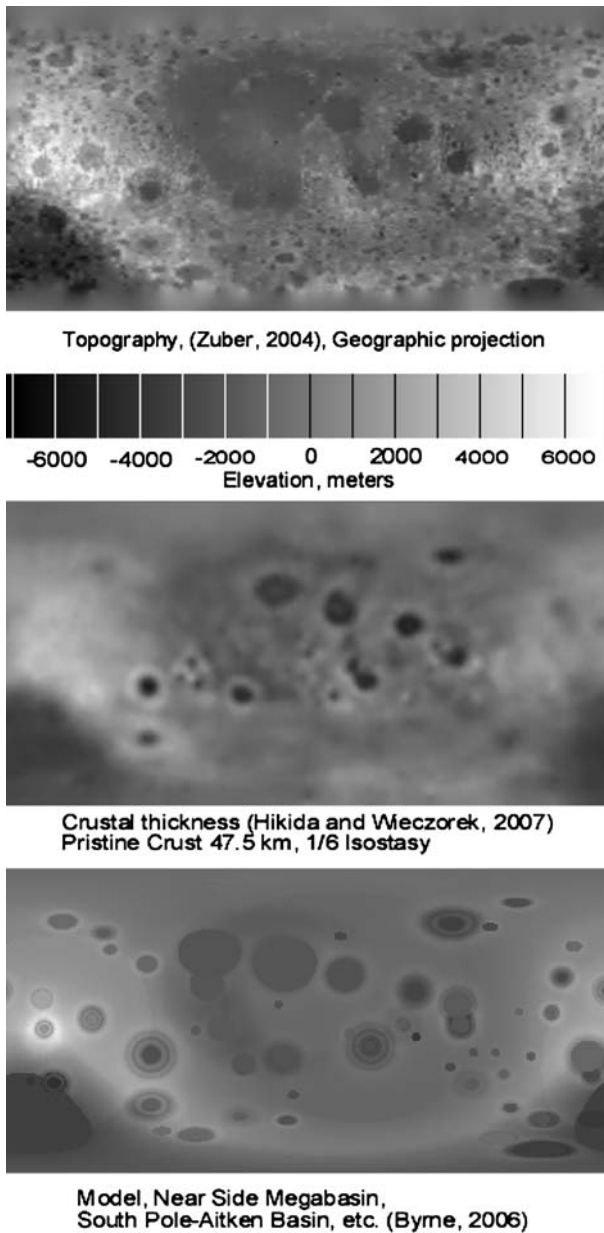
Fig. 21 The top map is the current topography. The middle map is the topography related to crustal thickness after isostosy. The bottom map is the model, including the Near Side Megabasin, the South Pole-Aitken Basin, and 52 other basins and large craters

In the map of current topography inferred from the crustal thickness map, the younger basins with mare fill stand out because they have not undergone full isostatic compensation.

The discussion topics raised in Sect. 7 need additional study and explanation from a multi-disciplinary view.

Improved elevation and gravity data, especially near the poles, would be helpful to sharpen the precision of the parameters of the Near Side Megabasin and the South Pole-Aitken Basin. The Lunar Reconnaissance Orbiter (Chin et al. 2006) is expected to provide such data. The ULCN 2005 has recently been released by the United States Geologic Survey (Archinal 2007) and provides data that includes and improves upon the Clementine LIDAR data used in this paper.

Appendix

Parameters and Variables

Symbol	Definition
D_A, R_A	Apparent diameter and radius at intersection of apparent cavity with the target surface (km)
d_T	True depth at the center of crater or basin after impact, before fill (m)
z_c	Depth of apparent cavity (m)
Z_c	Normalized depth of apparent cavity
R_m	1,738 (km)
G_m	1.622 (m/s^2)
v_i	Volume ejected (m^3)
V_i	Normalized volume ejected
V_0	Constant of incremental volume ejected
z_i	Internal ejected depth (m/s^2)
z_e	External depth of deposit (m/s^2)
z_0	Elevation before isostatic compensation (m)
z_{iso}	Elevation after isostatic compensation (m)
Z_i	Normalized internal ejected depth
Z_e	Normalized external depth of deposit
r_i	Actual radius internal to cavity (km)
r_e	Actual ejecta radius (km)
R_i	Normalized internal radius
R_e	Normalized radius, ejecta
s_i	Internal ejection speed (m/s)
S_i	Normalized internal ejection speed (m$^{-.5}$)
S_0	Constant of normalized speed
$F(R_i)$	Function of R_i that relates the speed to radius
exp	Exponent of ejection speed
A	Launch angle of ejection (°)
C	r_i/r_e, curvature corrected

Scaling Rules (Housen et al. 1983)

$$A = \text{constant}$$
$$r_i = R_A \cdot R_i$$
$$r_e = R_A \cdot R_e$$
$$z_i = d_T \cdot Z_i$$
$$z_e = d_T \cdot Z_e$$
$$s_i = R_A^{.5} \cdot S_i$$
$$F(R_i) \cong S_0 \cdot R_i^{-exp} \text{ for small } R_i \text{ (asymptote)}$$
$$V_i = V_0 \cdot R^3$$
$$v_i = V_e \cdot R_A^3$$

Ejecta Volume

Both the normalized volume and the actual volume of material that has been ejected up to the normalized or actual radius scales as the cube of that radius according to the dimensional analysis of Housen et al. (1983). This implies that the volume ejected from an incremental ring is scaled as the square of the radius.

This analysis assumes that this rule applies all the way to the rim, and it has not been found necessary to modify the rule.

In the analysis of the ejecta process, it is important to estimate the incremental volume of ejecta from an incremental ring of the radius (Ivanov 1986).

The derivative is easily derived from the scaling rule for total ejected volume:

$$dV_i/dR_i = V_0 \cdot R_i^2 \tag{A.1}$$

where V_i is the volume ejected from an incremental ring of the internal depression and V_0 is the constant of proportionality.

V_0 is determined by matching the calculated depth of ejecta deposits to the observed depth. Relating the volume of ejecta to that missing from the depression is an important constraint on the model but allowance should be made for the probable greater porosity of the ejecta.

Range of Ejecta

The range of the ejecta for typical basins is given by the familiar parabolic ballistic equation:

$$r_b = 2 \cdot (s_i^2/G_m) \tag{A.2}$$

where r_i is the range of deposit from the ejection radius, s_e is the magnitude of the velocity of ejection, and the angle of ejection is assumed to be 45°.

Since r_b is proportional to s_e^2 for the parabolic trajectory and speed is proportional to $R_A^{.5}$, then R_b scales with R_i for the parabolic trajectory:

$$R_b = R_A \cdot R_i \tag{A.3}$$

Then

$$R_e = R_i + R_b \tag{A.4}$$

Depth of Ejecta

The expression above implies that the normalized depth of material ejected from the surface of the depression can be found from:

$$Z_i \cdot 2 \cdot \pi \cdot dR_i = dV_i \tag{A.5}$$

where Z_i is the depth of material ejected from an incremental ring at a radius R_i. Note that Z_i is not the same as Z_c, the depth of the apparent crater after completion of the dynamic process of forming the transient crater and the collapse phase (body, Eq. 1).

$$Z_i = V_0 \cdot R_i^2 / (2 \cdot \pi) \tag{A.6}$$

The depth of deposited ejecta can be found from following the ring of ejecta from its radius of ejection to its radius of deposit, as determined by the range of the ballistic trajectory, R_b:

$$r_e = r_i + r_b \tag{A.7}$$

where r_i is the radius of ejection from the internal cavity and r_e is the radius of external deposit.

The range r_b is found in Eq. A.2.

The depth of ejecta as a function of R_e is found by equating the volume of ejecta leaving the internal cavity to the volume deposited externally (a change in porosity is neglected at this point):

$$Z_i \cdot 2 \cdot \pi \cdot R_i \cdot dR_i = Z_e \cdot 2 \cdot \pi \cdot R_e \cdot dR_e \tag{A.8}$$

where Z_e is the depth of the external deposit.

Solving for Z_e,

$$Z_e = Z_r (R_i / R_e) / (dR_e / dR_i) \tag{A.9}$$

The derivative of R_e with R_i can be calculated from Eq. A.4, given a final or trial velocity profile.

Ejection Velocity Profile

$$s_i = R_A^{0.5} \cdot S_i = R_A^{0.5} \cdot F(R_i) \tag{A.10}$$

where $F[R_i]$ is a function that relates normalized ejection speed to normalized internal radius.

Away from the rim (R_i somewhat less than 1),

$$S_i = S_0 \cdot R_i^{-\exp} \tag{A.11}$$

where S_0 is the constant of proportionality.

The constant S_0 and the exponent *exp* are to be determined empirically, along with V_0 and the shape of the velocity profile. Note that the speed of ejection is unlimited near the initial impact point, the center of the basin or large crater. The speed is actually limited during an initial phase of contact between the impactor and the target, which is neglected here.

Dimensional analysis does not provide a guide to the modification of the velocity function near the rim, and that is the most difficult aspect of forming a comprehensive basin model. The approach that led to a detailed velocity model near the rim (Fig. 9 of the body) was to work backward from the shape of the ejecta field of impact features to infer the velocity function that would have produced the observed radial profiles of ejecta. The equations of motion of the ejecta connect the radial profiles to the velocity function.

The detailed shape of the magnitude of the velocity function $F[R_i]$ shown in Fig. 9 was determined by trial and error to yield a reasonable analytic fit to the radial profiles of the ejecta from many lunar impact features.

The resultant function of normalized speed as a function of normalized radius is defined in segments.

For $0 \geq R_i \leq 0.7$:

$$S_f = 0.73 \cdot R_i^{-2.6} \tag{A.12}$$

For $0.85 < R_i \leq 0.99$:

$$S_r = (4.23 - 0.23 \cdot e^{(-(1-R_i)/.021)} - 3.74 \cdot R_i) \tag{A.13}$$

S_r falls rapidly to 0 between $R_i = 0.99$ and $R_i = 1$.

The gap between these two segments of the speed function is filled by a transition function.

For $0.71 \leq R_i \leq 0.84$:

$$S_g = (S_r + 10.44 \cdot (0.85 - R_i)^2) \tag{A.14}$$

The segments above are roughly divided according to the principle parts of the ejecta deposits. S_f is the part of the function that will form the far field, S_r is the part of the function that will form the rim, and S_g is the part of the function that will form the greater part of the ejecta blanket. The parameters 0.73 and 2.6 in Eq. A.10 are the values of S_0 and *exp* in Eq. A.11.

The far field segment of the speed function follows the form determined by dimensional analysis. It would be desirable if the equations for the other segments were to relate to physical reasoning of the evolving transient crater very near the rim. A recent contribution (Richardson 2007) is discussed in the body, after Eq. 3. The equations of this paper are analytic approximations that yield acceptable ejecta shapes. Experimental data on the ejection velocity in this region would be valuable.

Effect of the Curvature of the Moon

For megabasins like the South Pole-Aitken Basin or the Near Side Megabasin, the curvature of the Moon cannot be neglected. For example, an orbital equation must be used to find R_b (fortunately, there is no atmospheric drag on the Moon). Secondly, the circumference of the incremental ring where the ejecta lands is not simply proportional to the radius R_e as it is when curvature can be neglected. These effects not only must be

considered for accuracy but also change the qualitative nature of the ejecta patterns, as shown in Figs. 11, 14, and 15.

In the following analysis, the rotational speed of the Moon is neglected, although it is possible that the effects are significant, although modest. In any case, the rotation rate and position of the lunar axis are not known at the time of the impacts that left the Near Side Megabasin and the South Pole-Aitken Basin.

The ejecta is launched in either an elliptical orbit (if it returns to the Moon) or a hyperbolic trajectory (if it escapes). Then the range, if the ejecta cone does not escape, is given by:

$$r_b = 2R_m \tan^{-1} \left[\frac{(s_i^2/R_m \cdot G_m) \cdot \sin A \cdot \cos A}{1 - (s_i^2/R_m \cdot G_m) \cdot \cos^2 A} \right] \tag{A.15}$$

where r_b is the range between the radius of ejection and the radius of deposit, s_i is the ejection speed, R_m is the radius of the Moon, G_m is the Moon's gravity at its surface, and A is the angle of launch. The equation above is quoted in Melosh (1989) and the derivation is in Thomson (1986).

Once Eq. A.15 is used to find range, r_b can no longer be normalized on the apparent radius R_A, nor can r_e, since it depends on the range. Vertical measurements can still be normalized on the true depth.

Shrinking Circumference of the Landing Ring

The second step accounts for the changing circumference of the incremental ring where the ejected material lands. When curvature is neglected, the ratio of the launching circumference to the landing circumference is simply R_i/R_e, and the ejecta depth is multiplied by that ratio (Eq. A.9). However, when curvature is considered, the ratio of circumference becomes:

$$C = Sin(r_i/R_m)/Sin(r_e/R_m) \tag{A.16}$$

Then, from Eq. A.9,

$$Z_e = Z_r \cdot C/(dr_e/dr_i) \tag{A.17}$$

Note that C_r becomes infinite when $R_e = \pi \cdot R_m$, 180° around the Moon from the point of impact, the antipode of that point. Of course, the depth of ejecta is limited by dispersion due to the chaotic nature of the process because the angle of an ejection cone actually covers a narrow range around the average launch angle and the speed of launch is also distributed in a range of values. The dynamic angle of repose also limits the shape of the antipode mound.

Numerical Analysis

The final model of basins and large craters that was used to determine the parameters for the Near Side Megabasin included computations for trajectories influenced by the curvature of the Moon and the elliptical nature of the basin. An elevation map by radius and azimuth was calculated for a set of trial parameters. The normalized radius of the ejecta launch point was incremented by 0.01 up to 0.99 and then by 0.001 up to 1.0. Azimuth was

incremented by 1°. The normalizing radius R_s varied elliptically with azimuth. The depth of the internal depression was calculated from the negative cosine (Eq. 1 in the body of this paper). The depth of ejecta was calculated by substituting the formula for the range of ejecta (Eq. A.15) to find the deposit radius. Equation A.17 was used to compute the depth of ejecta.

The parameters for latitude, longitude, apparent radius of the major axis, true depth, eccentricity, and azimuth of the major axis, were then varied manually, seeking minimization of the standard deviation of the residual elevation map. This map was constructed by subtracting the sum of the depth of all of the impact models (Near Side Megabasin, South Pole-Aitken Basin, and 52 other basins and large craters) from the elevation map of topogrd1 (Zuber et al. 2004).

In the initial search for a large near side basin, the eccentricity was set at 0 and only a single basin was modeled. The full set of models was used to refine the parameters of the Near Side Megabasin and to assure that there was a major reduction in standard deviation.

Calculation of Standard Deviation

The standard deviation was calculated over the range of latitude from $-78°$ to $+78°$, excluding the polar regions because of the inaccuracy of the Clementine Lidar data in that range (Zuber et al. 1994).

The improvement in standard deviation due to modeling is summarized in Table 3 of the body. The standard deviation for the residual elevations is less than half of that of the current elevations of the far side of the Moon and just over half for the whole Moon. The features modeled included the Near Side Megabasin, its partially refilled layer of crust, the Oceanus Procellarum depression caused by mare depletion, the South Pole-Aitken Basin, and over 50 basins and large craters.

The residual standard deviation represents the remaining features that were not modeled (such as all of the medium and small craters), the great circle ring of heights, variations of the features from the models, and LIDAR errors.

The Relation Between Depth to Diameter

The measured diameter and depth of each basin in the sample for Fig. 6 of the body is shown in Table A.1. The dimensions are similar to published values (Wilhelms 1987; Spudis 1993) except for the Grimaldi Basin. In this case, the published data may have been based on an outer ring. Table A.1 also includes the Imbrium Basin (Fig. A.1) and the Serenitatis Basin, both deeply flooded with mare, for comparison.

In the following discussion, italicized terms are as defined in Turtle et al. (2005). The diameter is the *apparent diameter*, measured at the intercept of the cavity with the estimated original target surface. The depth is the estimated *true depth* at the center of the cavity from the estimated target surface (before mare or other fill). This depth (d_T) and the radius corresponding to the diameter (R_A) are used in normalizing the radial profiles and scaling the velocity and depth of ejecta.

Table A.1 Radial profiles of selected lunar basins

Name	Diameter (km)	Depth (m)
Grimaldi	210	1,850
Hertzsprung	520	5,200
Humboldtianum	624	4,000
Humorum	400	1,500
Imbrium	1,084	2,000
Korolev	396	6,400
Moscoviense	414	4,800
Orientale	888	4,650
Serenitatis	716	3,300

Fig. A.1 Radial profile of the Imbrium Basin
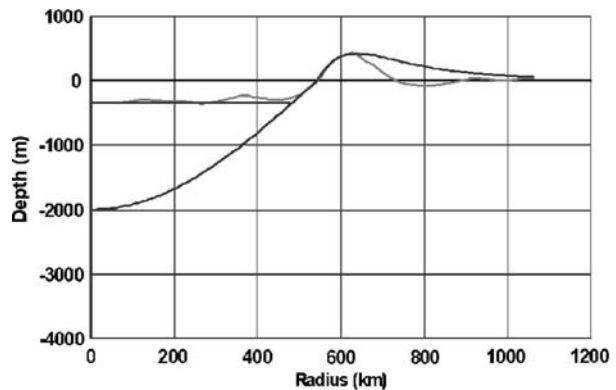
Two Large Basins

Estimates of the degree of isostatic compensation for a number of major basins and the depths of their original excavation cavities have been made from crustal thickness measurements (Wieczorek and Phillips 1999). This paper estimates only the current topographic depths for all but the Near Side Megabasin, the South Pole-Aitken Basin, and the Imbrium Basin.

Two basins that were found to be exceptional according to the crustal thickness analysis (Wieczorek and Phillips 1999) are the Imbrium Basin and the Serenitatis Basin, both found to be shallow for their size. The current topography of these two basins is also unusual (Figs. A.1, A.2).

The topographic profiles of these two basins, especially their rims, may be distorted by their mutual proximity (their rims actually overlap).

Depth Graphed Against Diameter

The data in Table A.1 is graphed in Fig. A.3. The "Near Side" basins, are those that have impacted the cavity of the Near Side Megabasin. The "Far Side" basins have impacted the deep ejecta from the Near Side Megabasin. The "Megabasins" are the South Pole-Aitken Basin and the Near Side Megabasin.

Fig. A.2 Radial profile of the Serenitatis Basin
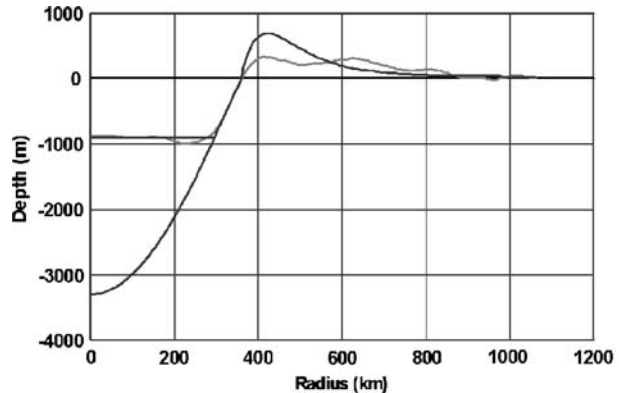
Fig. A.3 A log–log plot of depth versus diameter for the basins in Table A.1. Dots are "Near Side" basins, in the cavity of the Near Side Megabasin. Diamonds are "Far Side" basins, in ejecta from the Near Side Megabasin. The stars are the two "Megabasins". Vertical bars show the effect of isostatic compensation. The triangle is the Imbrium Basin
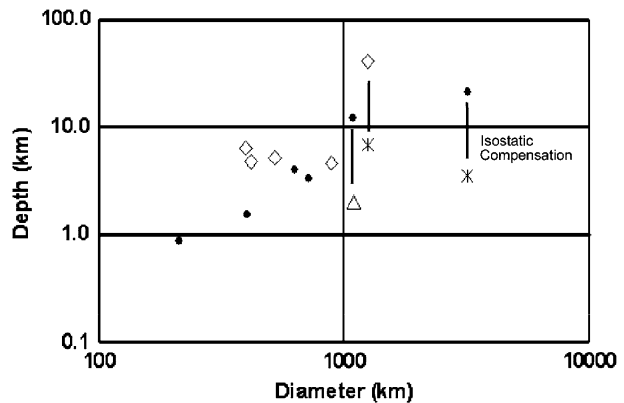
The vertical bars increase depth by a factor of 6, to show the depth just after impact of the Near Side Megabasin and the South Pole-Aitken Basin. This modification has also been made for the Imbrium Basin, which is in the KREEP terrane and may have experienced isostasy in the late Imbrium or Eratosthenian period, probably because the crust there was softened by the concentration of radioactive elements there.

With those modifications, the set of basins that were formed in low-porosity materials are reasonably well structured. The "Far Side" basins, including the South Pole-Aitken Basin (with isostasy restored) are deeper by a factor of about 2, probably because they impacted lower porosity target material.

Serenitatis is only a little shallower than other basin, but the topography of Imbrium is much shallower because it has apparently undergone isostatic compensation.

References

B.A. Archinal, Final completion of the Unified Lunar Control Network 2005 and the lunar topographic model, LPSC XXXVIII, Abstract 1904 (2007)

A.B. Binder, Lunar Prospector: overview. Science **281**, 1475–1476 (1998)

B. Bussey, P.D. Spudis, *The Clementine Atlas of the Moon*. Cambridge University Press (2004)

C.J. Byrne, Automated cosmetic improvement of mosaics from the Lunar Orbiter Atlas, LPSC XXXIII, Abstract 1260 (2002)

C.J. Byrne, Evidence for three basins beneath Oceanus Procellarum, LPSC XXXV, Abstract 1103 (2004)

C.J. Byrne, *Lunar Orbiter Photographic Atlas of the Near Side of the Moon*. Springer-Verlag, London (2005)

C.J. Byrne, Radial profiles of lunar basins, LPSC XXXVII, Abstract 1900 (2006a)

C.J. Byrne, The Near Side Megabasin of the Moon, LPSC XXXVII, Abstract 1930 (2006b)

C.J. Byrne, *The Far Side of the Moon: A Photographic Guide*. Springer-Verlag, New York (2008)

P.H. Cadogan, Oldest and largest lunar basin? Nature **250**(5464), 315–316 (1974)

G. Chin, A. Bartels, S. Brylow, M. Foote, J. Garvin, J. Kaspar, J. Keller, I. Mitrofanov, K. Raney, M. Robinson, D. Smith, H. Spence, P. Spudis, S.A. Stern, M. Zuber, Lunar reconnaissance Orbiter overview: the instrument suite and mission, LPSC XXVII, Abstract 1949 (2006)

R.C. Elphic, D.J. Lawrence, W.C. Feldman, B.L. Burraclough, O.M. Gasnault, S. Maurice, P.G. Lucey, D.T. Blewett, Lunar Prospector neutron spectrometer constraints on TiO_2. JGR **107**(E4), 5024 (2002), doi: 10.1029/2000JE001460

W.C. Feldman, O. Gasnault, S. Maurice, D.J. Lawrence, R.C. Elphic, P.G. Lucey, A.B. Binder, Global distribution of lunar composition: new results from Lunar Prospector. JGR **107**(E3), 5016 (2002), doi: 10.1029/2001JE001506

I. Garrick-Bethell, Ellipses of the South Pole-Aitken Basin: implications for basin formation, LPSC XXXV, Abstract 1515 (2004)

I. Garrick-Bethell, I.J. Wisdom, M.T. Zuber, Evidence for a past high-eccentricity lunar orbit. Science **313**, 652–655 (2006)

O. Gasnault, W.C. Feldman, C. d'Uston, D.J. Lawrence, S. Maurice, S.D. Chevrel, P.C. Pinet, R.C. Elphic, I. Genetay, K.R. Moore, Statistical analysis of thorium and fast neutron data at the lunar surface. JGR **107**(E10), 5072 (2002), doi:10.1029/2000JE001461

S.H. Hikida, H. Mizutani, Earth, planets, and space **57**, 1121–1126 (2005)

S.H. Hikida, M.A. Wieczorek, Crustal thickness of the Moon: new constraints from gravity inversion using polyhedral shape models, LPSC 2007, Abstract #1547 (2007)

K.R. Housen, R.M. Schmidt, K.A. Holsapple, Crater ejecta scaling laws: fundamental forms based on dimensional analysis. JGR **88**(B3), 2485–2499 (1983)

B.A. Ivanov, The effect of gravity on crater formation: thickness of ejecta and concentric basins. in *Proceeding of the Lunar Science Conference, 7th* (1976)

B.A. Ivanov, Lunar impact basins—numerical modeling, LPSC XXXVII, Abstract 2003 (2007)

B.L. Jolliff, J.J. Gillis, L.A. Haskin, R.L. Korotev, M.A. Wieczorek, Major lunar crustal terranes: surface expressions and crust-mantle origins. JGR **105**(E2), 4197–4216 (2000)

D.J. Lawrence, W.C. Feldman, B.L. Barraclough, A.B. Binder, R.C. Elphic, S. Maurice, M.C. Miller, T.H. Prettyman, Thorium abundances on the lunar surface. JGR **195**(E8), 20,307–20,331 (2000)

D.J. Lawrence, W.C. Feldman, R.C. Wlphic, R.C. Little, T.H. Prettyman, S. Maurice, P.G. Lucey, Iron abundances on the lunar surface as measured by the Lunar Prospector gamma-ray and neutron spectrometers. JGR **107**(E12), 5130 (2002), doi:10.1029/2001JE001530

P.G. Lucey, P.D. Spudis, M. Zuber, D. Smith, E. Malaret, Topographic-compositional units on the Moon and the early evolution of the lunar crust. Science **266**, 1855–1858 (1994)

P. Lucey, R.L. Korotev, J.J. Gillis, L.A. Taylor, D. Lawrence, B.A. Campbell, R. Elphic, B. Feldman, L.L. Hood, D. Hunten, M. Mendillo, S. Noble, J.J. Papike, R.C. Reedy, S. Lawson, T. Prettyman, O. Gasnault, S. Maurice, Understanding the lunar surface and space–Moon interactions in the book *New Views of the Moon*, reviews in mineralogy and geochemistry. Mineralogical Society of America **60**, 83–220 (2006)

H.J. Melosh, *Impact Cratering. A Geologic Process*. Oxford University Press (1989)

G.A. Neumann, M.T. Zuber, D.E. Smith, F.G. Lemoine, The lunar crust: global structure and signature of major basins. JGR **101**(E7), 16,841–16,843 (1996)

S. Nozette et al., The Clementine mission to the moon. Science **266**, 1835–1839 (1994)

N.E. Petro, C.M. Pieters, Surviving the heavy bombardment: ancient material at the surface of South Pole-Aitken basin. JGR **109**(E06004) (2004), doi:1029/2003JE002182

N.E. Petro, C.M. Pieters, The lunar-wide effects of the formation of basins on the megaregolith, LPSC XXXVI, Abstract 1209 (2005)

J.E. Richardson, Improving the modeling of impact ejecta behavior: the effects of gravity and strength near the crater rim, LPSC XXXVIII, Abstract 1345 (2007)

P.H. Schultz, A possible link between Procellarum and the South Pole-Aitken Basin, LPSC XXXVIII, Abstract 1839 (2007)

P.D. Spudis, *The Geology of Multi-ring Impact Basins*. Cambridge University Press (1993)

W.T. Thomson, *Introduction to Space Dynamics*. Dover (1986)

E.P. Turtle, E. Pierazzo, G.S. Collins, G.R. Osinski, H.J. Melosh, J.V. Morgan, W.U. Reimold, Impact structures: what does crater diameter mean? Geological Society of America, Special Paper **384**, 1–24 (2005)

E.A. Whitaker, The lunar procellarum basin, in multi-ring basins, LPSCP 12, Part A (1981)

M.A. Wieczorek, R.J. Phillips, The structure of lunar basins: implications for basin forming processes, LPSC XXIX, Abstract 1299 (1998)

M.A. Wieczorek, R.J. Phillips, The Porcellarum KREEP terrane. Implications for mare volcanism and lunar evolution. JGR **105**(E8), 20,417–20,430 (2000)

M.A. Wieczorek, R.J. Phillips, R.L. Korotev, B.L. Jolliff, L.A. Haskin, Geophysical evidence for the existence of the lunar Procellarum KREEP terrane, LPSC XXX, Abstract 1548 (1999)

D.E. Wilhelms, *The Geologic History of the Moon*. USGS Professional Paper 1384, US Government Printing Office, Washington, DC (1987)

K.K. Williams, M.T. Zuber, Meaurement and analysis of lunar basin depths from Clementine altimetry. Icarus **11**, 107–122 (1998)

J.A. Wood, Bombardment as a cause of the lunar asymmetry. The Moon **8**, 77–103 (1973)

M.T. Zuber, D.E. Smith, G.A. Neumann, The shape and internal structure of the Moon from the Clementine Mission. Science **266**, 1839–1843 (1994)

M.T. Zuber, D.E. Smith, G.A. Neumann, Topogrd2, web site of the University of Washington in St. Louis, http://www.wufs.wustl.edu/geodata/clem1-gravity-topo-v1/ (2004)